Proceedings of the
Annual Stability Conference
Structural Stability Research Council
Denver, Colorado, March 22-25 2022

Constrained finite element analysis with displacement mapping: application to thin-walled members with holes

Trung Hoang[1], Sándor Ádány[2]

Abstract
A widely used approach to understand and analyze the complex behavior of a structural member is to decompose the complex phenomenon into simpler ones. In thin-walled members the deformations are frequently decomposed into the following behavior modes: global distortional local-plate, shear and transverse extension. A practical realization of this approach is the constrained finite element method (cFEM). Whilst the cFEM is readily applicable for a wide range of problems, still, a disadvantage of the currently available cFEM is that it is based on a specific rectangular shell finite element. This imposes two major restrictions: (i) highly regular rectangular mesh is a must, and (ii) the potential benefits of the various available shell elements cannot be utilized. The aim of the reported research is to release these restrictions set by the cFEM-specific shell element. The idea is to use two discretizations and two corresponding basis function systems. One is an ordinary shell finite element discretization, the other is the specific cFEM discretization. The basis functions of the cFEM are transferred to the ordinary shell model, then the calculations are completed in the ordinary shell model but with using the cFEM basis functions. The key step is the transfer of the cFEM basis functions, which can be realized by mapping between the nodal displacements of the two shell models. In the paper the proposed method is briefly introduced and some proof-of-concept examples are presented, with a special focus on members with holes.

1. Introduction

Cold-formed members are frequently found with holes in their webs. Typically in low-rise buildings, cold-formed steel studs and joists are provided with slotted holes to accommodate electrical conduits (and other services). Steel box girders commonly have access holes for inspection drilled into the flange or web. In airplanes, holes can also be found in numerous structural details, e.g., in the ribs attached to the main spar of an airplane wing. In thin-walled cold-formed structures, elastic buckling and load-bearing capacity are closely related; holes' presence may promote unique elastic buckling modes that may affect buckling loads as well as collapse mechanisms at an ultimate limit state. Depending on the size, shape, and arrangement of the holes, such holes can reduce both buckling capacity and overall strength. Buckling is, thus, a crucial aspect of the behavior of thin-walled perforated cold-formed steel structures (PCFS).

[1] PhD student, Budapest University of Technology and Economics, <hoang.trung@emk.bme.hu>
[2] Professor, Budapest University of Technology and Economics, <adany.sandor@emk.bme.hu>

Numerous research projects have investigated members with holes during the last few decades, with many publications. The buckling behavior of PCFS sections depends not only on the reduction in cross-sectional properties but also on the stress concentration caused by perforations. As with ordinary cold-formed steel sections, PCFS sections may also buckle locally (L), distortionary (D), and globally (G) due to loading. Because of the wide variety of perforations and their sizes, it is difficult to directly define the critical buckling stresses of PCFS sections (Moen & Schafer, 2009). It is essential to understand and be able to analyze these buckling phenomena separately. For an ordinary cold-formed steel section, there are many proposed methods for modal decomposition from which generalize beam theory (GBT), constrained finite strip method, and constrained finite element method (cFEM) are the most widely known. For PCFS, several attempts have been made for a similar purpose.

For cold-formed steel columns and beams with holes, simplified methods for approximating global, distortional, and local critical elastic buckling loads were also developed and summarized in (Moen & Schafer, 2009). There are also numerical methods that have also been proposed specifically for the analysis of thin-walled members with holes. In (Yao & Rasmussen, 2011), finite strip method (more specifically: iso-parametric spline FSM) is proposed and applied to members with holes, especially when a large number of smaller holes are present in a regular distribution, such as in rack uprights. In (Cai & Moen, 2016) and (M. Casafont, J. Bonada, M.M. Pastor, 2016), GBT-based methods are presented with two different approaches; the first proposes to handle the perforated member as an assembly of simple sub-members and define the cross-section modes on the sub-members, the second proposes to define the cross-section modes using the unperforated cross-section shape while including the effect of holes. These methods are relatively complicated, and still, their applicability seems to become problematic as soon as the hole shape or hole pattern is complicated (e.g., curved holes). In (Ádány, 2017), the cFEM method for members with holes is proposed. Due to its specific rectangular finite element shape, only rectangular holes can precisely be modeled, and curved holes can be approximated with unnatural meshing configuration.

To overcome the limitation of cFEM in analyzing elastic buckling of members with holes, the 'Constrained finite element analysis with displacement mapping' is introduced. This paper aims (i) to present a brief concept of constrained finite element analysis with displacement mapping and (ii) to illustrate it by numerical examples in analyzing elastic buckling of thin-walled members with holes. For this purpose, the constrained finite element method with mapping will shortly be summarized in Section 2. Then numerical examples for handling members with the holes will be presented and discussed in Section 3.

2. Constrained finite element method with displacement mapping

2.1 The constrained finite element method

The constrained finite element method is a shell finite element method with modal decomposition capabilities. Through mechanical constraints, the buckling modes are separated. The application of the right mechanical criteria results in on alternative basis system for the displacement field that is defined by the finite element nodal degrees of freedom: the practical benefit is that the deformation spaces are separated.

If the constraints are applied to a member without any additional elements, the $\mathbf{d}$ displacement vector can be expressed by the $\mathbf{d_M}$ modal displacement vector and the $\mathbf{R_M}$ constraint matrix specific to a given M deformation space, as:

$$\mathbf{d} = \mathbf{R_M d_M} \tag{1}$$

The buckling problem, mathematically, requires the solution of a generalized eigen-value problem, as follows:

$$\mathbf{K_e \Phi} - \mathbf{K_g \Lambda \Phi} = \mathbf{0} \tag{2}$$

where $\mathbf{K_e}$ and $\mathbf{K_g}$ are the elastic and geometric stiffness matrices, $\mathbf{\Lambda}$ contains the eigen-values (i.e., critical load multipliers), and $\mathbf{\Phi}$ contains the eigen-vectors (i.e., buckled shapes). Whenever modal decomposition is applied to a linear buckling problem, Eq. 1 is substituted into Eq. 2, which leads to another generalized eigen-value problem, given in the reduced M deformation space, as follows:

$$\mathbf{R_M}^{\mathrm{T}} \mathbf{K_e R_M \Phi_M} - \mathbf{R_M}^{\mathrm{T}} \mathbf{K_g R_M \Lambda \Phi_M} = \mathbf{0} \tag{3}$$

The benefit of modal decomposition is that the calculation is in a reduced (i.e., constrained) deformation space, and these deformation spaces can be pre-defined, as described above. For example, the linear buckling analysis can be done for the L deformations only by applying Eq. 1, meaning that all the buckled shapes will meet the mechanical criteria of L deformations; in other words, all the buckled shapes will be local. The calculation in a constrained deformation space is realized by selecting only those modal basis vectors that belong to the desired deformation mode space.

The cFEM is based on a specific shell element with a specific set of shape functions. The specific shape functions were chosen so that the mechanical criteria would be satisfied within each shell element and that the mechanical criteria would be exact. For detailed information, see (Ádány, 2018) and (Ádány et al., 2018). This is a nice feature of the existing cFEM procedure, which contributes to the precision and numerical stability of the calculations. However, the specific cFEM shell element is a flat rectangular element; it is suitable for many classic thin-walled steel problems but not always the best. That is why our effort is to make the constraining technique more general, i.e., constraining with ordinary shell finite elements.

2.2 The mapping procedure

The key idea of the constrained finite element method, which requires specific shape functions, is the modal decomposition which results in the separation of the deformation spaces. If we want to apply a generic shell element, the specific shape functions are not an option. One possible approach to – at least approximately – overcome this contradiction is mapping. The idea is to approximate the analyzed domain using two different discretizations, i.e., two different sets of basis functions. For one of the discretizations, an ordinary shell element is used; the basis functions, therefore, are determined by the shape functions of the selected ordinary shell element. For the other discretization, the specific cFEM shell elements are used; from this, an alternative basis function system is generated by using the shape functions of the cFEM shell element. In the former basis system, the stiffness matrices, load vectors, etc., are generated, and technically speaking, the

solution is obtained in the ordinary basis system. However, if modal decomposition is intended, the specific cFEM basis system, i.e., the basic functions of a constrained space, is mapped into the ordinary basis system, which means that the separated deformation space can now be generated in the ordinary basis system (e.g., if only the global basis functions are selected, then the solution can be obtained directly for the global modes).

A physical domain is approximated using the ordinary shell finite element, its basis system is denoted as (u^1, u^2, u^3, ..., u^m) from which a deformation *u*-space is defined. Another basis system based upon constrained shell finite element discretization can be used for the same (or similar) physical domain: the deformation space that is generated by this system is denoted as a *x*-space $(x^1, x^2, x^3, \dots, x^n)$. Let us assume that the *x*-space can be mapped into the *u*-space as:

$$x^i = x^i(u^1, u^2, u^3, \dots, u^m) \tag{4}$$

Once the explicit form of Eq. 4 is defined, any $\mathbf{d}(x^1, x^2, x^3, \dots, x^n)$ displacement vector in the *x*-space can be mapped into the *u*-space as a displacement vector $\mathbf{d}(u^1, u^2, u^3, \dots, u^m)$. It is worth mentioning that it is more convenient to use a similar but not necessarily identical physical domain in the cFEM basis system in some problems. As in the case of PCFS members, holes can be disregarded, and the cFEM discretization can be done on the unperforated member.

For mapping procedures, two techniques are employed in this paper. In the first approach, which is referred to as the *non-condensation mapping*, at *i*-th node in the ordinary element basis system, the displacement of that node, i.e., its degrees of freedom, are calculated directly from the displacements expressed in the cFEM nodal displacements and the cFEM shape functions. Consider the X degree of freedom (e.g., U, V, W, ROTX, ROTY, ROTZ, which correspond respectively to translations in *x*, *y*, *z*, and rotations around *x*, *y*, *z* axes) at the *i*-th node in target element basis, i.e., the ordinary element basis. Then its value can be calculated as:

$$\boldsymbol{X^i} = f(d_{cFEM}, (x_i, y_i, z_i), \{N_{cFEM}\}) \tag{5}$$

in which $\boldsymbol{X^i}$ is the degree of freedom (DOF) of the *i*-th node in the ordinary base, d_{cFEM} is the displacement vector in cFEM base, (x_i, y_i, z_i) is the coordinate of the *i*-th node and $\{N_{cFEM}\}$ is the set of shape functions of the cFEM element. The f operator is, indeed, the calculation of the displacements (e.g. *U*, *V*, *W*, etc…) of a point at the position (x_i, y_i, z_i) using cFEM shape functions.

In the second approach, henceforth referred to as the *condensation mapping*, the degrees of freedom u^i of the *i*-th node in the ordinary element basis system are separated into two groups: a translational one, i.e., *U*, *V*, *W*, which are the translations in *x*, *y*, and *z* axes of the *i*-th node, respectively; and a rotational one, i.e., *ROTX*, *ROTY*, *ROTZ*, which are the rotational of *i*-th node about *x*, *y*, and *z* axes.

For the *X* degree of freedom, which belongs to the translational group $\mathbf{d_T}$, the $\boldsymbol{X^i}$ is calculated in a similar manner as in the *non-condensation mapping* technique, using Eq. 5. For the remaining rotational $\mathbf{d_R}$ degrees of freedom in $\mathbf{d}(u^1, u^2, u^3, \dots, u^m)$, static condensation is adopted as follows:

$$\begin{bmatrix} \mathbf{K}_{e,tt} & \mathbf{K}_{e,tr} \\ \mathbf{K}_{e,rt} & \mathbf{K}_{e,rr} \end{bmatrix} \begin{bmatrix} \mathbf{d_T} \\ \mathbf{d_R} \end{bmatrix} = \begin{bmatrix} \mathbf{f_T} \\ 0 \end{bmatrix} \tag{6}$$

in which $\mathbf{d_T}$ is the translational displacement vector in the ordinary basis, $\mathbf{d_R}$ is the rotational displacement vector in the ordinary basis, and $\mathbf{K}_{e,tt}$, $\mathbf{K}_{e,rr}$, $\mathbf{K}_{e,tr}$ and $\mathbf{K}_{e,rt}$ are the partitions of the elastic stiffness matrix. From the second equation of Eq. 6 $\mathbf{d_R}$ can be expressed (formally) as:

$$\mathbf{d_R} = (\mathbf{K}_{e,rr})^{-1}(-\mathbf{K}_{e,rt}\mathbf{d_T}) \tag{7}$$

In the cFEM, modal decomposition generates the $\mathbf{R_M}$ constraint matrix, of which each of its column is considered as a displacement vector. The $\mathbf{R_M}$ contains '*r*' displacement vectors that form the basis vectors for the given 'M' deformation space. Accordingly, the above-described mapping procedure can transform $\mathbf{R_M}(x^1, x^2, x^3, \dots, x^n)$ in the *x*-space into the *u*-space as $\mathbf{R_M}(u^1, u^2, u^3, \dots, u^m)$ **.** As a result of this transformation, the constraint matrix $\mathbf{R_M}$ can possibly be expressed in the *u*-space of the ordinary shell, and the constraint analysis can readily be performed within the *u*-space, i.e., the steps of the constrained linear buckling problem follow Eq.1, 2, and 3, respectively.

2.3 Ordinary shell elements

As described in the previous Section, ordinary shell elements are required to map the cFEM basis functions. This paper employs an ordinary shell finite element, denoted as QUAD8. These elements are created by combining a 2D membrane element and a plate element based on the Reissner- Mindlin plate theory. It is an 8-node general quadrilateral element with 6 DOF per node, see Fig 1. Accordingly, local parametric coordinate systems are employed within the element, and the calculation of the element stiffness matrix is completed by numerical integration. It is worth pointing out that all these features contrast with the cFEM shell element, which must be rectangular, which is based on the Kirchhoff-Love plate theory, and in which analytical integration is used in the stiffness matrix formation.

It is to note that the implementation of our QUAD8 element is generated using the second-order Serendipity shape functions family, which is practically identical with the ANSYS shell281 element (ANSYS, 2018).

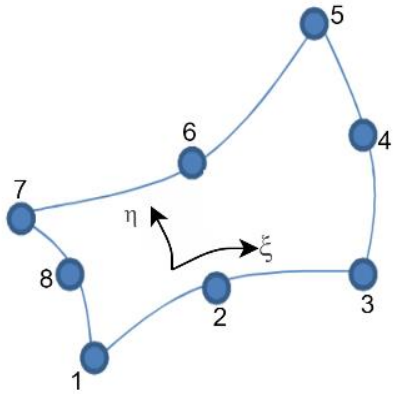

Figure 1: Demonstration of QUAD8 quadrilateral element.

3. Numerical examples

In this Section numerical examples are presented to illustrate the concept and potential of the proposed constrained analysis with mapping. Linear elastic isotropic material model is adopted for all the examples, with a modulus of elasticity of 210 GPa and Poisson's ratio of 0.3. Linear buckling analyses are conducted for a 1000 mm channel section with a uniform thickness of 1 mm. The channel depth is 100 mm, with 60 mm flange widths and 10 mm lip length. Nine evenly placed circular holes are inserted into the web with a radius of 40 mm, and 10 mm apart from each other along the member length. At the member ends, 100 mm are left without perforation. Unconstrained and constrained buckling analyses are conducted on the member which is fixed at one end; at the other end only the longitudinal deformation is allowed, and a uniform normal distributed load is applied. This example closely follows the one presented in (Duan et al., 2022), however, with the differences that the applied load is a uniform distributed force instead of the uniform displacement load, and that quadratic finite elements are used instead of linear ones.

3.1 Comparison unconstrained and constrained analyses

In (Duan et al., 2022) study, the first few buckled shapes of the similar member are mostly the combination of distortional buckling modes and local modes with small percentages of other buckling modes at those cross-sections close to member ends. So that, the constrained buckling analysis is performed with restriction to distortional-local space, i.e., only L, D, and their combination are occurred.

The unconstrained analysis is performed both by ANSYS with quadratic shell finite element and by our own software using QUAD8 elements. The total number of elements is 7879 and 7824, respectively. As indicated in the previous Section, the constrained analysis with displacement mapping requires a cFEM discretization together with a target QUAD8 discretization. For cFEM discretization, the member is treated as a common channel, i.e., the holes are ignored, with 574 elements in total.

In Table 1, the critical loads of the first five buckling modes obtained by ANSYS shell 281 finite element analysis and QUAD8 shell finite element analysis and the constrained finite element analysis with displacement mapping are presented. This analysis uses the condensation mapping technique. Note that the ANSYS shell 281 and QUAD8 are practically identical; though the meshes are not identical, the number of elements can be considered the same. Expectedly, the critical loads are practically identical, with the first five modes' differences being less than 0.1%. The critical load of the constraining to LD buckling shows systematically higher values; the differences are varied from 1.32% to 6.31%. These results are as expected, since in the unconstrained analysis there are certain other modes that appear in the buckled shape in addition to the local and distortional mode, e.g., transverse extension modes, shear modes. However, in the constrained analysis the buckling is forced to distortional-local buckling only; consequently, the member behaves slightly stiffer than the unconstrained one, leading to slightly higher critical loads. The results also suggest that in those modes in which the local buckling is governing the discrepancy is smaller than in those with governing distortional buckling.

The corresponding buckled shapes are shown in Fig. 2a-e. It is worth mentioning that the unconstrained buckled shapes in the case of ANSYS shell 281 and QUAD8 are exactly identical; only the ANSYS buckled shapes are shown here.

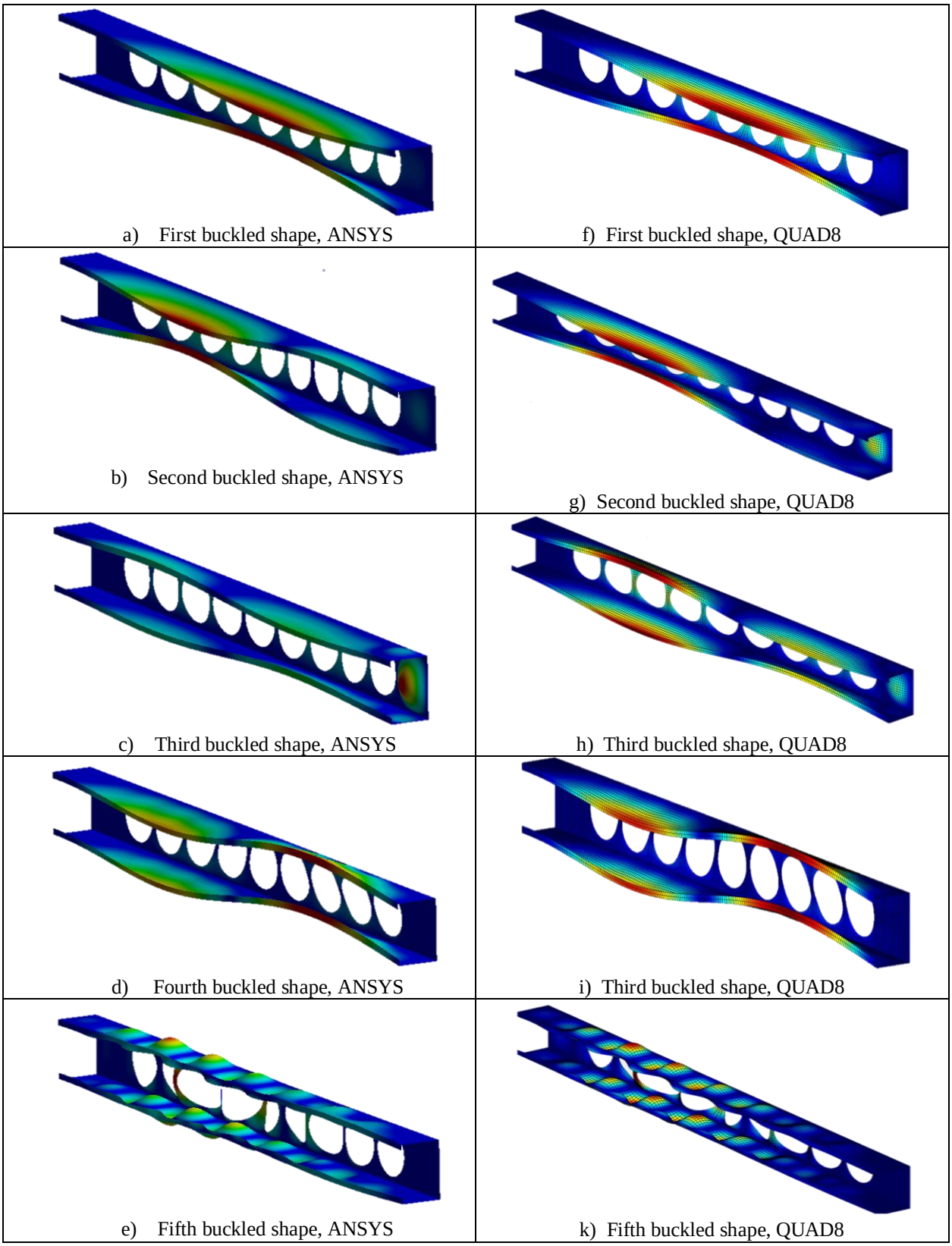

a) First buckled shape, ANSYS

f) First buckled shape, QUAD8

b) Second buckled shape, ANSYS

g) Second buckled shape, QUAD8

c) Third buckled shape, ANSYS

h) Third buckled shape, QUAD8

d) Fourth buckled shape, ANSYS

i) Third buckled shape, QUAD8

e) Fifth buckled shape, ANSYS

k) Fifth buckled shape, QUAD8

Figure 2: Buckled shapes of the member subjects to axial compressive load, unconstrained analysis with ANSYS shell 281 (a-e) and constrained to distortional-local buckling QUAD8 (f-k)

It can be seen in the buckled shapes of unconstrained analysis, the first, second, and fourth modes are governed by distortional modes. The first buckling mode is a symmetrical mode with a single half-wave, the second mode is also a symmetrical mode but with two half-waves, the fourth mode is a point symmetrical mode with two half-waves. In the third mode, the local buckling of the unperforated web is obviously more visible compared to other modes. The fifth buckled mode is governed by local buckling, which can be clearly seen in the flanges and the web. As the buckled shapes of the constrained analysis are concerned, they are very similar to the unconstrained ones. This observation confirms that these unconstrained modes are mostly combinations of local and distortional modes.

Table 1: Critical load of member subjected to axial compressive force: constrained and unconstrained buckling analysis

	Critical load [kN]				
	mode 1	mode 2	mode 3	mode 4	mode 5
ANSYS shell281	22.69	25.93	27.96	36.37	39.72
QUAD8	22.70	25.92	27.95	36.33	39.75
Constrained to LD space	23.61	27.54	28.66	38.62	40.27
Relative difference	3.98%	6.24%	2.53%	6.31%	1.32%

3.2 Effect of mesh configurations

With adequately selected cFEM discretization and ordinary QUAD8 discretization, the constrained finite element method with displacement mapping shows reasonable linear buckling analysis results. Since two independent mesh configurations are involved in the mapping procedure, it is essential to know the effect of each mesh on the accuracy of analysis results. The previous example is repeated with systematically arranged discretization schemes in cFEM and ordinary QUAD8. There are four different mesh configurations for cFEM discretization, of which the mesh density is a parameter corresponding to 110, 220, 330, 574 elements, see Fig. 3a-d. In ordinary QUAD8 discretization, a similar manner is established with four different mesh densities corresponding to 672, 1296, 2680, and 7824 elements, see Fig. 3e-h. Linear buckling analyses are performed, and the first ten buckling modes are collected: both critical loads and buckled shapes.

In Table 2 the results are displayed. The relative difference between the constrained critical loads with the unconstrained one, i.e., the difference between the critical load of the constrained and unconstrained one over the unconstrained critical load, are summarized as an average value of the first ten modes. Each row shows how the ordinary discretization affects the accuracy of the constrained analysis. Similarly, each column represents the effect of cFEM discretization. The results clearly show that the denser the ordinary mesh or the cFEM mesh, the more accurate results can be archived. The results also indicate that the ordinary mesh has slower improvement in the accuracy compared to the cFEM mesh. For example, in the first row, the difference between oF3 and oF4 is only 0.5% with approximately four times number of element. In contrast, with the first column, the difference between cF1 and cF3 is roughly 10% with only three times increasing of total element number. Though, this observation alone is not necessarily true for all types of problems.

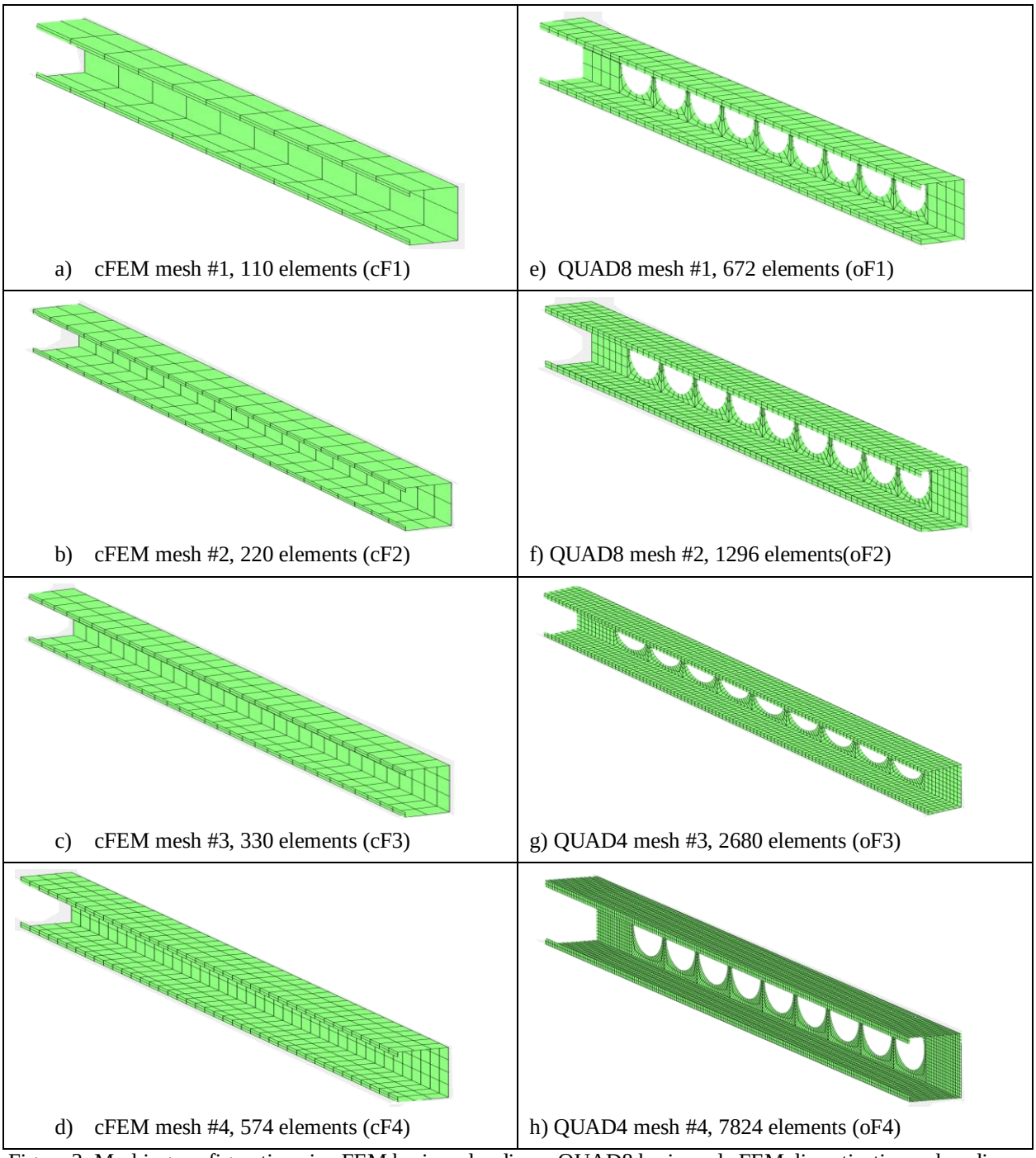

a) cFEM mesh #1, 110 elements (cF1)
e) QUAD8 mesh #1, 672 elements (oF1)
b) cFEM mesh #2, 220 elements (cF2)
f) QUAD8 mesh #2, 1296 elements(oF2)
c) cFEM mesh #3, 330 elements (cF3)
g) QUAD4 mesh #3, 2680 elements (oF3)
d) cFEM mesh #4, 574 elements (cF4)
h) QUAD4 mesh #4, 7824 elements (oF4)

Figure 3: Meshing configurations in cFEM basis and ordinary QUAD8 basis: a-d cFEM discretization, e-h ordinary QUAD8 discretization.

Table 2: Effect of different discretization schemes on the mapping critical loads.

	oF1	**oF2**	**oF3**	**oF4**
cF1	16.7%	15.3%	14.6%	14.1%
cF2	8.0%	6.2%	5.6%	5.3%
cF3	6.7%	4.7%	3.8%	3.5%
cF4	5.2%	3.3%	3.0%	2.7%

Table 3: Relative different critical loads constraining to local-distortional buckling, cF4 discretization scheme

	oF1	**oF2**	**oF3**	**oF4**
Mode 1	8.3%	5.3%	4.1%	4.0%
2	8.1%	6.3%	6.2%	6.2%
3	3.3%	3.3%	2.7%	2.5%
4	7.8%	6.7%	6.5%	6.3%
5	5.5%	1.9%	1.6%	1.3%
6	3.3%	1.9%	1.6%	1.4%
7	3.5%	1.9%	1.6%	1.3%
8	4.1%	1.9%	1.6%	1.4%
9	4.4%	2.2%	2.0%	1.7%
10	4.4%	2.1%	1.6%	1.3%

In Table 3 critical loads of the first ten modes of the linear buckling analyses, in which the constrained analysis is performed with a cF4 discretization scheme in cFEM base and four different ordinary QUAD8 discretization schemes, are shown. Each value in the table is a relative difference of constrained critical load and unconstrained one with identical discretization. It is worth noting that these differences are cumulative from 2 sources: the inaccuracy introduced by the mapping approximation procedure and the constraining itself. Although the distortional and local modes govern the unconstrained buckling deformation, there is a small contribution from other modes, e.g., transverse extension and shear modes, too.

According to the results, it is clear that the denser mesh yields closer to the unconstrained critical load. It is logical as the denser ordinary discretization approximates better the displacement space to which the buckling is constrained. It can be seen that the differences are more significant in the first four modes; note that distortional buckling governs these modes. Then it significantly drops from mode #5 to mode #10, where local buckling is governing.

The discretization schemes not only affect the critical load but also has an impact on the buckled displacement shapes. Fig. 4 and Fig. 5 show the buckled shapes of the first and fifth modes. In Fig. 4 the cFEM discretization scheme is the coarsest mesh cF1, see Fig. 3a, while in Fig. 5 the finest cFEM discretization scheme cF4 is selected, see Fig. 3d. In both figures, the ordinary QUAD8 discretization schemes oF1 cases are presented in the left column, and in the right one, the oF4 cases are shown (the coarsest and the most refined mesh ordinary QUAD8 discretization). It can be observed that the first buckled shapes are practically identical with all discretization settings and also identical to the first unconstrained buckled shape in Fig. 2a. However, the fifth buckled shapes of the constrained analysis are firmly dependent on the discretization setting; the coarse cFEM and ordinary discretization are the less likely local buckled shapes shown up, the finer cFEM and ordinary discretization, the closer to unconstrained buckled shape. Only in Fig. 6d (the most refined cFEM discretization and the ordinary QUAD8 discretization), the buckled shape is similar to the unconstrained one, as shown in Fig. 2e.

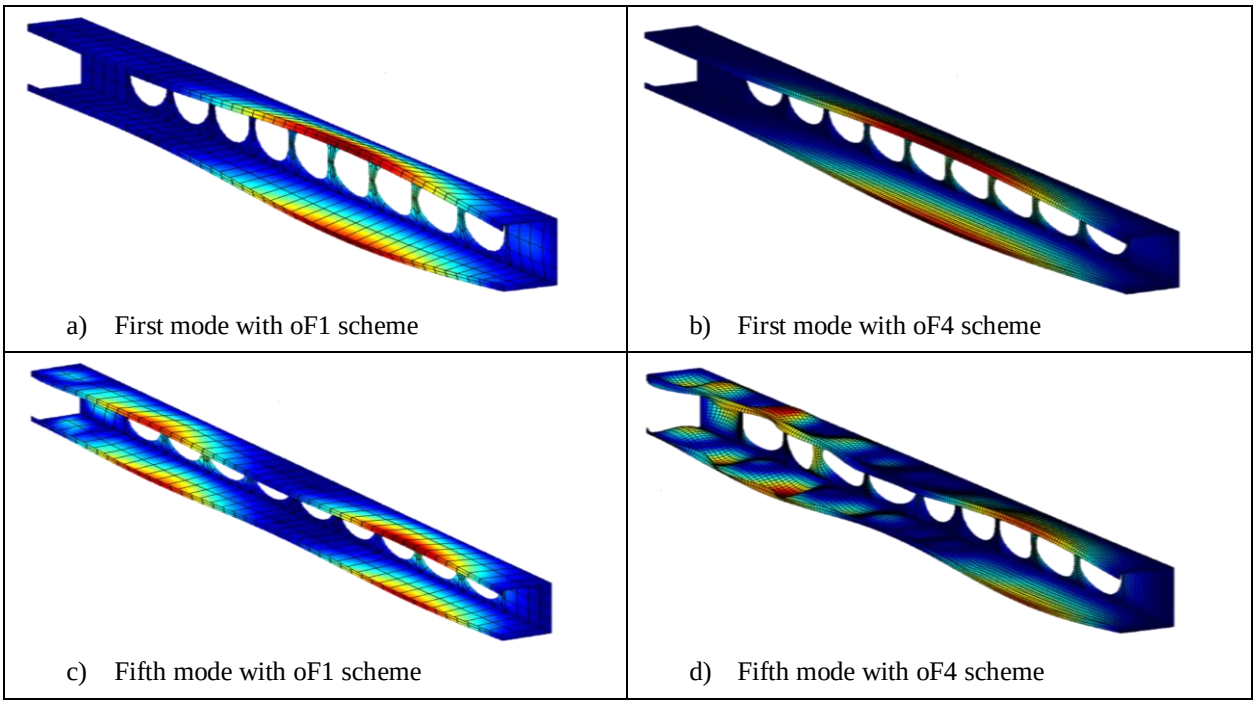

a) First mode with oF1 scheme

b) First mode with oF4 scheme

c) Fifth mode with oF1 scheme

d) Fifth mode with oF4 scheme

Figure 4: Buckled shapes of the constrained analysis with cF1 scheme for cFEM mesh

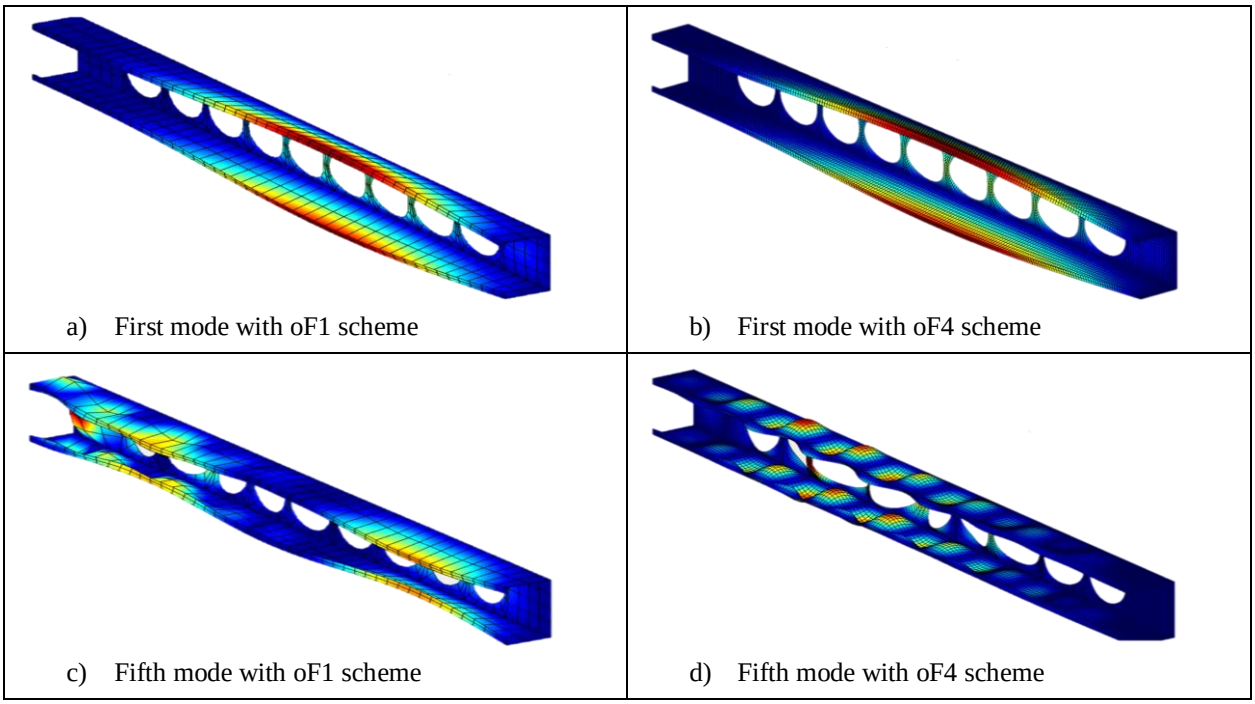

a) First mode with oF1 scheme

b) First mode with oF4 scheme

c) Fifth mode with oF1 scheme

d) Fifth mode with oF4 scheme

Figure 5: Buckled shapes of the constrained analysis with cF4 scheme for cFEM mesh

3.3 Constraining to global, distortional, and local spaces

The same member with the perforated web is analyzed with constraining to global, distortional and local buckling separately. In this analysis, only the densest mesh in both discretization schemes are chosen, i.e., cF4 in cFEM and oF4 in ordinary base. In order to capture the effect of holes on

the buckling behavior of the member, the analyses of the identical member without holes are performed; the analyzed results are compared to the linear buckling analysis of the identical member but without holes. Buckling analysis of the member without holes is conducted with the original cFEM software; critical loads and buckled shapes are both collected.

In Table 4, critical loads of the first buckling modes are presented for the member with the perforated web and the critical load of the member without perforation. The associated buckled shapes are collected in Fig. 6.

The appearance of holes on the web does not change the nature of the buckling phenomenon in the case of pure G, D, and L buckling, i.e., the buckled shapes remain (nearly) the same, see Fig. 6a-f, though it significantly reduces the global buckling critical load and the distortional buckling critical load. This result is logical and expected since it is well-known that the cross-section inertia has an essential role in the global buckling resistance; with the appearance of holes, the cross-section inertial is reduced significantly, which results in 22% less critical load. This fact is also the main reason for the reduction of the distortional buckling critical load; since the out of plane deformation of the web has an important role in the distortional behavior of the member, it is obvious that the significant number of holes on the web reduces its ability to resist the out of plane deformation that is why the distortional buckling critical load is decreasing.

While having a negative impact on global and distortional buckling resistance, the perforation on the web has an impressive positive impact on the local buckling resistance of the member. Local buckling critical load increases about 17% with the perforated web compared to the unperforated one. The authors believe that stress redistribution in the perforated web is the main contributor to this effect; with the missing material in the position of the hole, stresses in the web is carried through the relatively small part close to the web-flange junction, which has much stronger resistance to buckling compared to the plate buckling resistance of the web in case of an unperforated member.

One important feature of the constrained finite element method is that buckling spaces can easily be combined. In this example, the combination of G+D, G+L, D+L modes analyses are conducted. For G+D and G+L analysis, there is no surprise that the first buckling mode of G+D is a distortional buckling, and the first buckling mode of G+L is local buckling, regardless of the appearance of holes. For the L+D mode analysis, however, the appearance of holes just slightly reduces the critical load of the first buckling mode, 1% reduction. A dramatic change occurs in buckled shape in the member with holes; the first buckling mode of a member without holes is clearly the local buckling of the web plate, while in the case of a perforated member, it is a distortional one, see Fig.7g-h.

Table 4: First critical buckling load with different constraining space

	G	**D**	**L**	**G+D**	**G+L**	**D+L**
Unperforated [kN]	229.31	41.02	23.89	40.93	23.89	23.84
Perforated [kN]	176.69	33.39	28.01	33.31	28.23	23.61
Effect of holes [%]	-22.95%	-18.61%	17.26%	-18.62%	18.19%	-1.00%

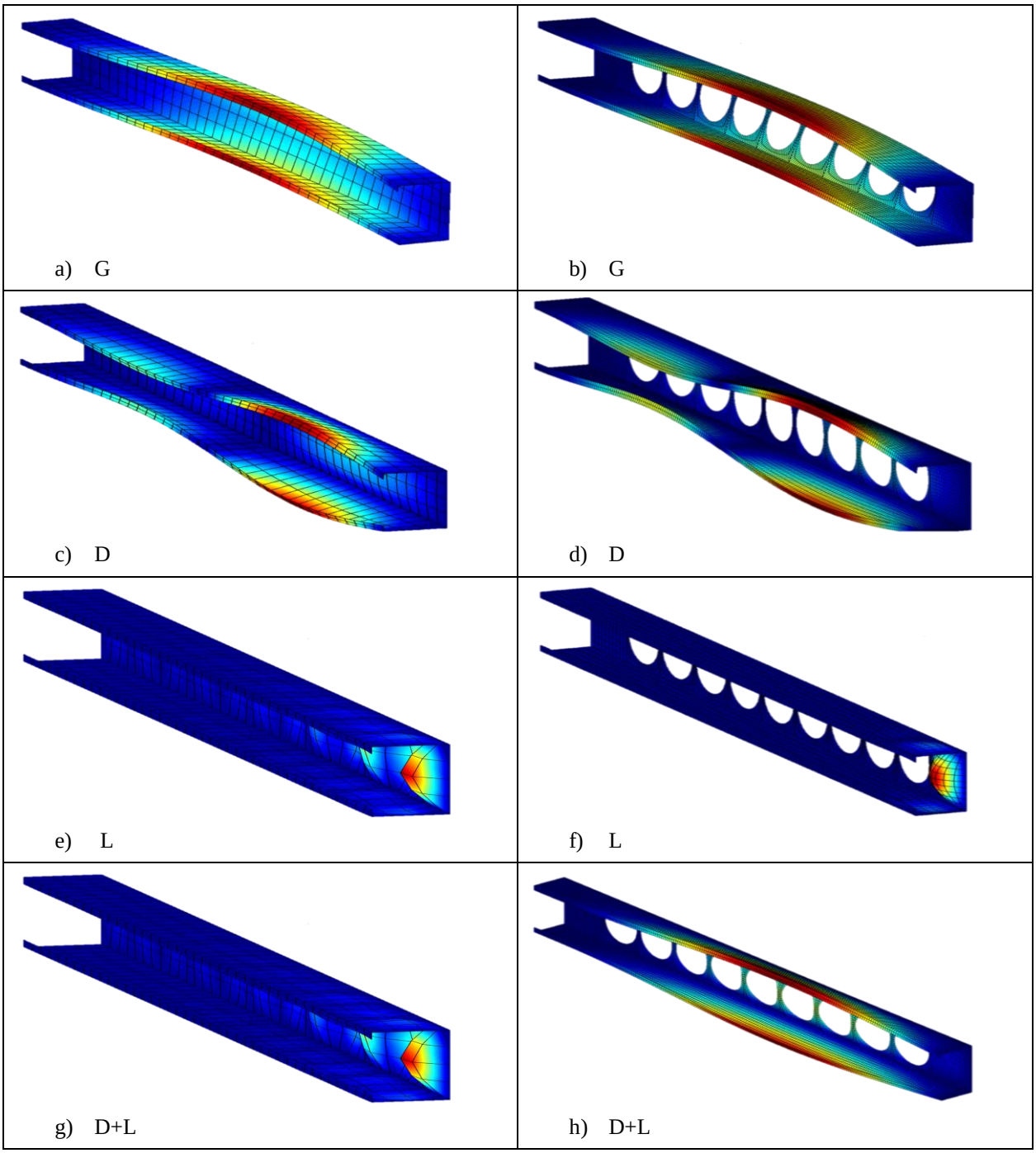

Figure 6: First buckled modes with constrained buckling analysis: (a) (c) (e) (g) unperforated members, (b) (d) (f) (h) perforated members.

3.4 Condensation vs non-condensation mapping technique

In this Section the constrained analyses of the same member are conducted with constraining into distortional-local space as performed in Section 3.1. The change is that the non-condensation technique, which has been introduced in Section 2.2, is used now. The cFEM discretization scheme

is set to the cF4 options, and in the ordinary basis, discretization scheme is a parameter with oF1-oF4 options.

The critical loads of the first five buckling modes are collected in Table 5 and Table 6, both condensation and non-condensation technique results are presented with various QUAD8 discretization schemes, from left to right the mesh density is increasing. In Table 5 the absolute critical values, in Table 6 the relative differences compared to the unconstrained buckling critical loads, i.e., a relative difference is calculated as a constrained critical load minus the unconstrained critical load relative to the unconstrained value, are displayed. From Table 5 and especially Table 6, it can be seen that, with a proper dense mesh, e.g., oF3 or oF4, the condensation and non-condensation yield practically the same results, though the non-condensation results are still slightly higher than the condensation one. In the case of coarse mesh, the non-condensation yields a much higher critical load than the condensation one, technically speaking, with coarse ordinary discretization the results of non-condensation mapping are not reliable. The main explanation is that in the non-condensation technique, all DOFs of the nodes are forced to deform according to the pre-defined cFEM modal functions, while only the translation DOFs are forced to in the condensation technique. This fact indeed results in a more flexible system in the case of condensation and consequently a slightly lower critical load.

Table 5: Critical loads [kN] of the member subjects to axial load: constraining to distortional local buckling with condensation and non-condensation mapping technique.

	Non-condensation				**Condensation**			
Mesh scheme	oF1	oF2	oF3	oF4	oF1	oF2	oF3	oF4
Mode 1	28.03	25.03	23.96	23.77	25.76	24.33	23.76	23.61
2	30.58	28.50	27.80	27.71	28.73	27.78	27.59	27.54
3	37.30	29.59	28.89	28.81	29.65	28.91	28.71	28.66
4	43.60	40.31	39.27	39.00	40.90	39.19	38.78	38.62
5	47.38	42.68	41.13	40.77	43.81	40.81	40.41	40.27

Table 6: Relative difference of the constrained critical loads [%] compared to the unconstrained ones: constraining to distortional-local buckling with condensation and non-condensation mapping technique.

	Non-condensation				**Condensation**			
Mesh scheme	oF1	oF2	oF3	oF4	oF1	oF2	oF3	oF4
Mode 1	17.84%	8.30%	5.02%	4.68%	8.28%	5.28%	4.14%	3.98%
2	15.08%	9.03%	6.99%	6.87%	8.12%	6.27%	6.18%	6.24%
3	28.64%	5.76%	3.38%	3.05%	2.26%	3.31%	2.73%	2.53%
4	14.88%	9.71%	7.82%	7.33%	7.79%	6.66%	6.45%	6.31%
5	14.11%	6.58%	3.37%	2.57%	5.53%	1.90%	1.59%	1.32%

4. Summary

This paper introduces the method of constrained finite element analysis with displacement mapping. The conceptual details of the proposed method and proof-of-concept numerical examples are shown. The proposed method shows its ability to perform the constrained analysis with an ordinary shell finite element. Especially for a perforated member, i.e., a channel member with circular holes in the web plate, the proposed method has overcome the limitation of the

original cFEM of the rectangular element with promising results. The proposed method has shown good analysis results with properly selected discretization schemes. Comparison to commercial ANSYS software results has been made, which validates the proposed method. Some remarks from the numerical examples are listed as follows:

i. The discretization schemes in both cFEM and ordinary QUAD8 basis have an essential impact on the accuracy of the buckling analyses. The denser the discretization is, the better accuracy is achieved.
ii. Two variants of the displacement mapping technique was proposed, and both work well with properly selected discretizations. The condensation technique often results in a lower critical value due to loose links between cFEM and ordinary basis.
iii. The conducted numerical studies show that the appearance of holes reduces the member's global and distortional buckling resistance while it can increase the local buckling resistance. Also, the appearance of holes can transform the nature of the buckling phenomena in the channel member. All these observations are in accordance with earlier findings, which justify the applicability of the proposed method.

Acknowledgements

The presented work was partially supported by two projects of the National Research, Development and Innovation Office (TKP2020 NC, Grant No. BME-NCS and K138615).

References

Ádány, S. (2017). Constrained shell finite element method for thin-walled members with holes. *Thin-Walled Structures*, *121*(August), 41–56. https://doi.org/10.1016/j.tws.2017.09.021

Ádány, S. (2018). Constrained shell Finite Element Method for thin-walled members, Part 1: constraints for a single band of finite elements. *Thin-Walled Structures*, *128*(January), 43–55. https://doi.org/10.1016/j.tws.2017.01.015

Ádány, S., Visy, D., & Nagy, R. (2018). Constrained shell Finite Element Method, Part 2: application to linear buckling analysis of thin-walled members. *Thin-Walled Structures*, *128*(January), 56–70. https://doi.org/10.1016/j.tws.2017.01.022

ANSYS. (2018). ANSYS 19.1 Release Notes. *Ansys, Inc.*, *April*.

Cai, J., & Moen, C. D. (2016). Elastic buckling analysis of thin-walled structural members with rectangular holes using generalized beam theory. *Thin-Walled Structures*, *107*, 274–286. https://doi.org/10.1016/j.tws.2016.06.014

Duan, L., Zhao, J., & Zou, J. (2022). Generalized beam theory-based advanced beam finite elements for linear buckling analyses of perforated thin-walled members. *Computers and Structures*, *259*, 106683. https://doi.org/10.1016/j.compstruc.2021.106683

M. Casafont, J. Bonada, M.M. Pastor, F. R. (2016). No Title. *GBT Calculation on Elastic Buckling Loads of Cold-Formed Steel Rack Columns*, 297–304.

Moen, C. D., & Schafer, B. W. (2009). Elastic buckling of thin plates with holes in compression or bending. *Thin-Walled Structures*, *47*(12), 1597–1607. https://doi.org/10.1016/j.tws.2009.05.001

Yao, Z., & Rasmussen, K. J. R. (2011). Material and geometric nonlinear isoparametric spline finite strip analysis of perforated thin-walled steel structures - Analytical developments. *Thin-Walled Structures*, *49*(11), 1374–1391. https://doi.org/10.1016/j.tws.2011.06.005